Sensors and Materials, Vol. 38, No. 4 (2026) 2203–2215
MYU Tokyo

S & M 4431

Kurtosis-guided Adaptive Wavelet Thresholding Method for Enhancing Fault Feature Extraction in Advanced Vibration Sensors

Xinrong Liu*

School of Computer Science and Technology, Shandong Technology and Business University, Yantai 264003, China

(Received January 29, 2026; accepted April 1, 2026)

Keywords: bearing fault diagnoses, fault feature extraction, wavelet threshold, algorithm, envelope spectrum

Rolling bearings are essential components in rotating machinery. Harsh operating conditions frequently lead to the structural failure of bearings caused by mechanical vibration. While advanced vibration sensors capture high-fidelity data, the resulting signals are obscured by significant background noise, hindering the extraction of incipient fault features. To address the challenges of early-stage fault detection in industrial environments, a smart sensing framework that integrates an adaptive signal-processing layer directly into advanced vibration sensors was developed. This framework utilizes a kurtosis-guided adaptive wavelet thresholding method to transform raw, noisy sensor data into high-fidelity diagnostic information at the sensing node. By embedding intelligence and advanced sensors, the limitations caused by background noise can be addressed while preserving critical fault-related transients, facilitating autonomous edge-based diagnostics. By integrating the signal kurtosis and the decomposition level into the thresholding function, the algorithm adaptively suppresses noise while preserving the integrity of fault-related transients. To validate the approach, a simulation model was established with an inner ring fault frequency of 100 Hz and a carrier frequency of 2000 Hz, augmented with real-world noise extracted from the Case Western Reserve University data. The algorithm isolates the fault frequency and its corresponding harmonics at 200 and 300 Hz, whereas variational mode decomposition and standard wavelet thresholding do not accurately identify these harmonic markers in high-noise environments. This algorithm and the research results provide an efficient signal-processing framework essential for the development of smart sensors used for edge-based, early-stage fault diagnostics.

1. Introduction

Rolling bearings are critical components in rotating machinery, and their reliable operation is essential for industrial productivity. Bearings are frequently used in harsh operating environments that can cause structural degradation and failure.[1,2] Statistical analyses indicate

*Corresponding author: e-mail: 201511764@sdtbu.edu.cn
https://doi.org/10.18494/SAM6264

ISSN 0914-4935
https://myukk.org/

that approximately 65% of mechanical failures are vibration-induced, with 30% of these failures originating from bearing defects.[3] Therefore, robust, efficient, and accurate fault detection methods to prevent defects and failures are essential.[4]

To address these challenges, smart vibration sensors are required in industrial IoT. Being different from traditional transducers, advanced sensing nodes operate in integrated frameworks for localized data interpretation to reduce transmission bandwidth and improve diagnostic accuracy. The framework demands a kurtosis-guided adaptive wavelet thresholding method designed for the functional enhancement of these sensors. By embedding the method into the data acquisition layer, sensors can autonomously suppress background noise while preserving incipient fault-related transients, effectively transforming a raw vibration transducer into an intelligent diagnostic tool.[5] The challenge in acoustic and vibration-based sensing is not the capture of data, but distinguishing the signal of a fault from the noise of the machine's operation.

While existing frameworks use static thresholds that might suppress the faint, impulsive sounds of early-stage bearing wear, it is necessary to identify these sharp, transient fault markers. This necessitates an adaptive smart filter that utilizes statistical properties. By integrating this logic into the sensing process, microscopic structural failures can be detected before they become catastrophic, thereby extending the functional life and reliability of the sensing system in harsh industrial environments.[6]

The accuracy of fault diagnosis is closely linked to sensor technology. While advanced high-frequency accelerometers and MEMS are used to capture abnormal vibrations, the raw data provided by the sensors is interfered with by high levels of background noise.[7] Therefore, in using advanced sensors, sophisticated signal processing algorithms are required to isolate fault-related features from the noise.[8] Therefore, the extraction of fault-related data from raw sensor signals has been extensively researched.[9]

For the accurate extraction of data, various feature extraction techniques have been used. A compound fault detection algorithm utilizing hierarchical operator morphological wavelets and local feature amplitude ratios is used to isolate individual fault signals,[10] but its complexity in real-time monitoring hinders its widespread application. This leads to the introduction of wavelet threshold denoising with empirical mode decomposition (EMD).[11] However, EMD often yields inaccurate results owing to mode mixing or aliasing. Variational mode decomposition (VMD) has also been applied to enhance the filtering ability.[12] However, using VMD frequently fails to capture the associated harmonic frequencies in the presence of significant noise, although it identifies fault frequencies more accurately than using wavelet analysis. Although integrating modified wavelet thresholding with fast spectral kurtosis has shown promise for fault detection,[13] its significant computational demands make it inappropriate for deployment on resource-constrained sensor nodes.

The loss of harmonic information significantly degrades the accuracy, completeness, and prognostic capability of the diagnostic system. To solve such problems, algorithms to accurately detect harmonic signals alongside the fundamental fault frequency in high-noise environments must be created. Such algorithms must discern imprecise fault classification and severity assessment. Different bearing components (inner ring, outer ring, or rolling elements) exhibit distinctive harmonic distribution patterns. For example, outer ring faults manifest even-order

harmonics, while rolling element faults exhibit specific fractional-order characteristics. Without identifying these harmonics, fault types cannot be accurately isolated nor can the degree of deterioration from early-stage wear to late-stage failure be evaluated. In the incipient stages of damage, the fault frequency is weak and masked in noise. However, higher-order harmonics act as characteristic markers for such early faults. Therefore, using only the fundamental frequency results in missing opportunities for early intervention. Also, industrial environments are characterized by nonperiodic interference, such as electromagnetic noise from motors. These interference signals lack regular harmonic structures, which is different from general bearing faults. The absence of harmonic isolation leads to false positives, where external noise is misidentified as a mechanical fault.

In this study, we developed an algorithm for fault feature extraction tailored specifically for advanced sensors. Whereas regular sensors act as passive transducers requiring external high-capacity processors, advanced sensors (or smart sensors) incorporate embedded processing units and high-sensitivity MEMS or piezoelectric sensing elements. These advanced sensors are capable of localized data refinement at the point of measurement. The framework developed in this study contributes to the design of next-generation sensors by providing a mathematically efficient denoising logic that can be integrated into the sensor's firmware.[14] By enabling the sensor to autonomously differentiate between mechanical noise and fault-related transients, the algorithm developed in this study facilitates simple data collection for real-time, edge-based diagnostic sensing.

2. Fault Feature Extraction

2.1 Signal decomposition

To analyze bearing vibration signals, we used ensemble empirical mode decomposition (EEMD) to prevent mode mixing by averaging decompositions of signals with added white noise. EEMD is an improved version of EMD, which was designed to overcome mode mixing. It adds small amounts of white noise to the signal multiple times, performs EMD on each noisy signal, and then averages the results. The added noise cancels out statistically, but the averaging process helps separate signal components more clearly. As a result, EEMD produces more reliable intrinsic mode functions (IMFs) than standard EMD, especially for complex vibration signals suach as those in fault diagnosis.[6]

EEMD produces several IMFs ordered by frequency. Since bearing faults mainly appear in high-frequency vibrations,[9] we focused on the high-frequency IMFs and discarded the low-frequency ones. To refine the decomposition, we applied the average standardized accumulated mode (ASAM) method.[15] ASAM helps distinguish high-frequency IMFs (values close to zero) from low-frequency ones. The ASAM value is defined in Eq. (1), and IMFs classified as high frequency were used for signal reconstruction.

$$m = mean\left(\sum_{i=1}^{n}\left(IMF_i - \frac{mean\left(IMF_i\right)}{std\left(IMF_i\right)}\right)\right) \tag{1}$$

Here, m represents the ASAM value of IMF_1 to IMF_n, *mean*(·) is an averaging function, and *std*(·) represents the standard deviation of the values.

2.2 Kurtosis

Kurtosis is used to measure the sharpness of a signal and is sensitive to impulsive events, making it useful for detecting bearing faults [Eq. (2)].[16] A kurtosis value lower than 3 indicates normal operation, while values above 3 suggest damage, with higher values corresponding to more severe faults.[17] In the method developed in this study, kurtosis was used to select high-frequency components with strong fault signatures for reconstruction.

$$kurtosis\left(x\right)=\frac{\frac{1}{n}\sum_{i=1}^{n}\left(x_i-\overline{x}\right)^4}{\left(\frac{1}{n}\sum_{i=1}^{n}\left(x_i-\overline{x}\right)^2\right)^2} \tag{2}$$

Here, n represents the total number of samples in the discrete signal, x_i represents the amplitude of individual data points, and $\overline{x}$ represents the mean amplitude of the sampled signal. As a dimensionless statistical indicator, kurtosis is sensitive to the sharp, impulsive peaks caused by bearing surface defects, making it an ideal parameter for guiding the adaptive thresholding process in advanced sensing nodes.[18]

2.3 Improved wavelet thresholding

Wavelet thresholding is widely used for noise reduction. In this study, the threshold calculation was modified to emphasize fault features. Instead of applying a uniform threshold, we adjusted it adaptively using the kurtosis and frequency of each wavelet coefficient. The soft thresholding function is defined as Eq. (3).[19,20] The conventional minimax threshold is shown in Eq. (4), with the standard deviation term σj computed using Eq. (5). In the method developed in this study, the threshold was modified using kurtosis, as expressed in Eq. (6). This adaptive approach ensures that high-frequency coefficients with strong fault information are retained while noise is suppressed. Unlike conventional methods that preserve low-frequency components, the algorithm developed in this study discards them to highlight fault-related details.

$$g_j=\begin{cases}\mathrm{sgn}(p_j)\left(\left|p_j\right|-\lambda_j\right), & \left|p_j\right|\geq\lambda_j\\ 0. & \left|p_j\right|<\lambda_j\end{cases} \tag{3}$$

Here, g_j represents the thresholded coefficient, p_j denotes the j-th high-frequency coefficient obtained from wavelet decomposition, and λ_j is the threshold corresponding to g_j. The threshold

value is calculated using the minimax method, expressed as

$$\lambda_j = \begin{cases} \sigma_j \left(0.1829 \times \dfrac{\ln L}{\ln 2} + 0.3969 \right), & L > 32 \\ 0, & L \le 32 \end{cases} \tag{4}$$

where L denotes the signal length, and σ_j is the standard deviation of p_j, computed as follows.

$$\sigma_j = \frac{median\left(\left| p_j \right| \right)}{0.6745}, \tag{5}$$

$$\lambda_j = \begin{cases} \sigma_j \left(0.1829 \times \dfrac{\ln L}{\ln 2} + 0.3969 \right) \left(\dfrac{j}{kurtosis\left(p_j \right)} \right), & L > 32 \\ 0. & L \le 32 \end{cases} \tag{6}$$

Here, $kurtosis(p_j)$ denotes the kurtosis of the coefficient p_j.

The constants used in these equations (0.1829, 0.3969, 0.6745) originate from statistical estimation theory and experimental optimization.[21] For wavelet decomposition, the high-frequency detail coefficients with smaller values of j correspond to higher frequencies.[22] This adaptive approach ensures that high-frequency coefficients with strong fault information are retained while noise is suppressed. Unlike conventional methods that preserve low-frequency components, the developed algorithm discards them to highlight fault-related details.

The overall process is summarized as follows.

- Decompose the vibration signal using EEMD
- Identify high-frequency IMFs using ASAM [Eq. (1)]
- Reconstruct the signal from selected IMFs
- Apply the improved wavelet thresholding method [Eqs. (3)–(6)], guided by kurtosis [Eq. (2)]
- Reconstruct the final signal, emphasizing fault-related features

Figures 1 and 2 illustrate the workflow and process of the proposed algorithm. This streamlined description highlights the essential steps while retaining the mathematical definitions for readers who want the technical detail.

3. Simulation Results

The simulation was designed for the data acquisition process of an advanced vibration sensor. The variable x represents the ground truth or denoised reference signal obtained from the Case Western Reserve University (CWRU) database, providing a clean baseline of a real inner ring fault. To simulate a harsh industrial environment, n denotes the empirical residual noise isolated from raw experimental data. These were combined to form s, the composite noisy signal that serves as the input to the framework. In the processing stage, R represents the reconstructed high-frequency signal formed by combining the specific IMFs identified as signal-dominant by

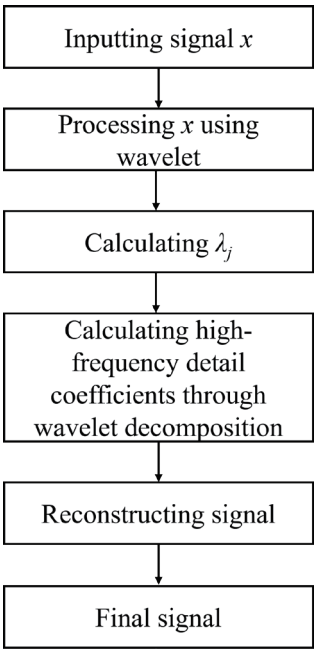

Fig. 1. Workflow of wavelet threshold algorithm developed in this study.

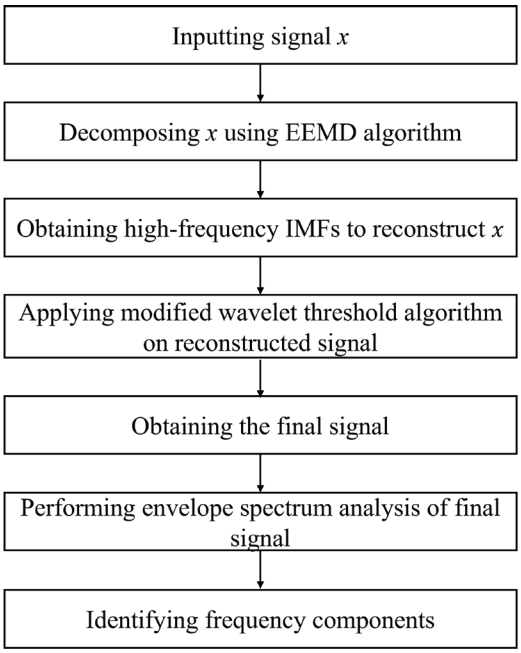

Fig. 2. Process of wavelet threshold algorithm developed in this study.

the ASAM criteria. w is the resulting smart output after the adaptive wavelet thresholding is applied to R and is then used for the final diagnostic envelope spectrum analysis.

To validate the developed algorithm, a mathematical model representing the vibration signal of a rolling bearing with an inner ring pitting fault was established. The localized defect causes periodic impulses that modulate a high-frequency resonance (carrier) signal. The modulation model is expressed as[23]

$$x(t) = \left(U + V\cos\left(2\pi f_i t\right)\right)\cos\left(2\pi f_c t\right), \tag{7}$$

where f_i is the fault characteristic frequency of the inner ring, f_c is the carrier resonance frequency, $V\cos(2\pi f_i t)$ represents the modulating test signal, U is the DC bias component, and $\cos(2\pi f_c t)$ denotes the high-frequency carrier signal.

In this simulation, the parameters are set to f_i = 100 Hz and f_c = 2000 Hz, with amplitudes U = V = 1. To replicate realistic industrial conditions, the simulated signal is augmented with an additive noise component, $n(t)$, yielding the final composite fault signal $s(t)$.[24]

$$s\left(t\right) = x\left(t\right) + n\left(t\right) \tag{8}$$

To ensure high fidelity in the simulation, the noise signal $n(t)$ was derived from empirical data rather than purely synthetic white noise. The source data is obtained from the CWRU Bearing Data Center, which is a benchmark repository for bearing fault diagnosis. In the

extraction process, a standard wavelet denoising algorithm was applied to a raw inner ring fault signal, $o(t)$, collected from the CWRU data.[25] The residual noise was isolated by subtracting the denoised signal, $x(t)$, from the original observation as follows.[26]

$$n(t) = o(t) - xd(t) \tag{9}$$

The equations reflect the complex, non-Gaussian background noise encountered in actual mechanical systems in simulation. Figures 3 and 4 show the waveforms of $x(t)$ and $n(t)$, respectively, and Fig. 5 presents the waveform of $s(t)$.

The signal $s(t)$ was decomposed using the EEMD algorithm, yielding ten IMF components. Figure 6 presents the waveforms of the first seven IMFs obtained through EEMD. The ASAM values were then calculated using Eq. (1), with the results for the first seven IMFs summarized in Table 1. The results indicate a sudden and significant change beginning at IMF3, while IMF1 and IMF2 remain close to zero. Consequently, IMF1 and IMF2 are identified as high-frequency components. These two components are subsequently used to reconstruct the signal, denoted as R.

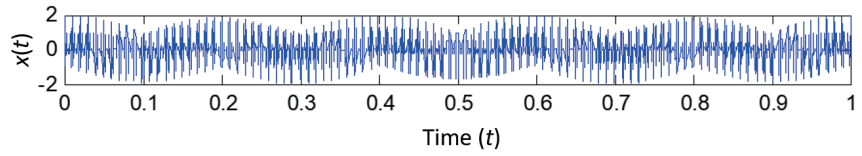

Fig. 3. (Color online) Waveform of $x(t)$.

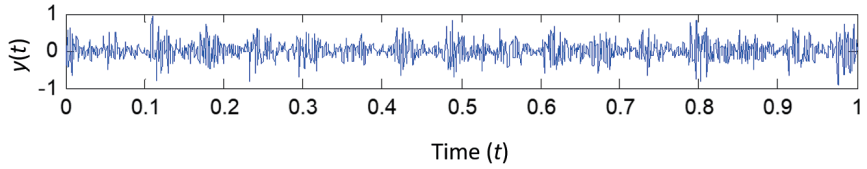

Fig. 4. (Color online) Waveform of $n(t)$.

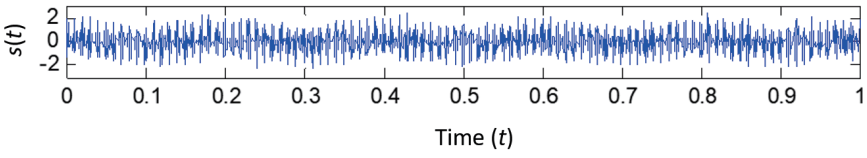

Fig. 5. (Color online) Waveform of $s(t)$.

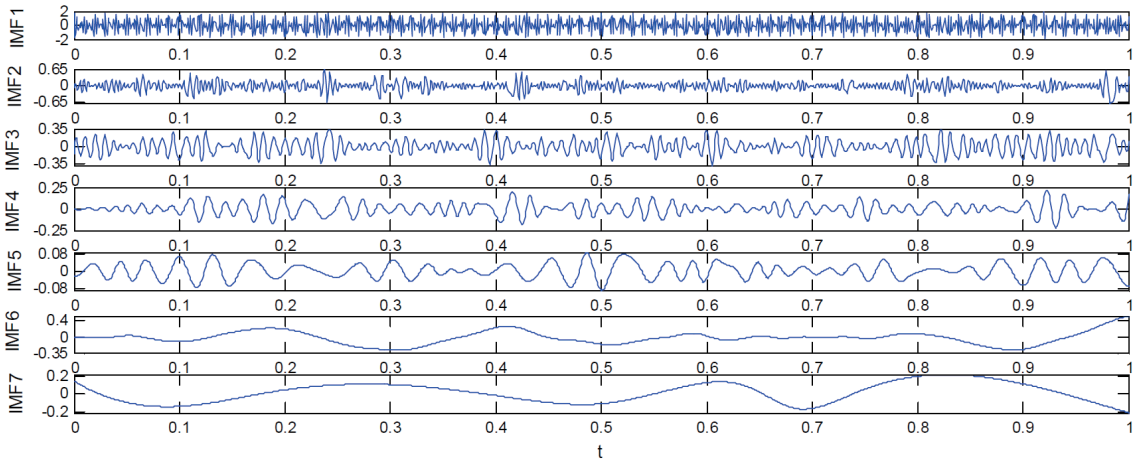

Fig. 6. (Color online) Waveforms of EEMD results.

Table 1
Calculation results for decomposition of signals.

	IMF1	IMF2	IMF3	IMF4	IMF5	IMF6	IMF7
ASAM ($\times 10^{-2}$)	0.029	0.025	3.31	3.66	0.67	8.11	−5.97

The modified wavelet threshold algorithm is applied to the reconstructed signal R, yielding the final signal w. Figure 7 illustrates the waveform of R, while Fig. 8 presents the waveform of w. During the algorithm's execution, a five-level wavelet decomposition is performed on R. The threshold corresponding to each high-frequency coefficient was calculated using Eq. (6).

The signal w is subjected to envelope spectrum analysis, and the corresponding spectrum is shown in Fig. 9. As observed, the pulse waveform near the fault frequency of 100 Hz is clearly visible, along with its second (200 Hz), third (300 Hz), and fourth (400 Hz) harmonics. Figure 10 presents the envelope spectrum of $y(t)$, which was not processed using the developed algorithm. Although the fault signal at around 100 Hz was identifiable, the harmonic components were not distinguished. This demonstrates that the detection results were affected by noise and that the extraction of fault features is incomplete. In comparison, the algorithm developed in this study revealed the fault frequency and its higher-order harmonics. This indicated that fault feature extraction was significantly improved and that the influence of noise was effectively suppressed. Consequently, the developed algorithm accurately detected fault features.

4. Bearing Fault Detection

4.1 Inner ring fault

The CWRU data was used in this study. In the simulation, we used a power tester, a two-horsepower motor, and a torque sensor. The drive-end bearing was SKF6205, while the fan-end bearing was SKF6203. The sampling frequency was set to 12 kHz (Table 2).

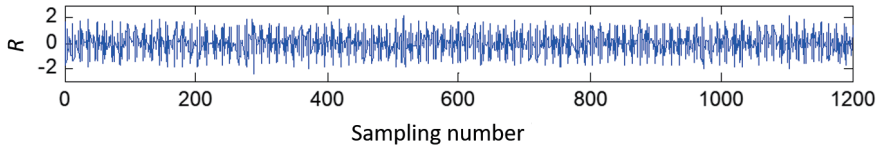

Fig. 7. (Color online) Waveform of *R*.

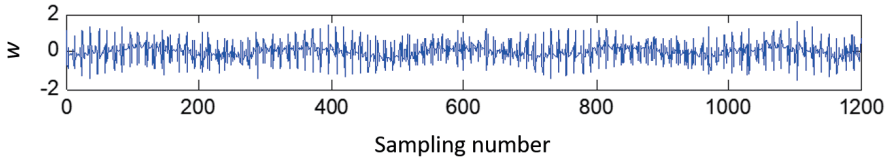

Fig. 8. (Color online) Waveform of *w*.

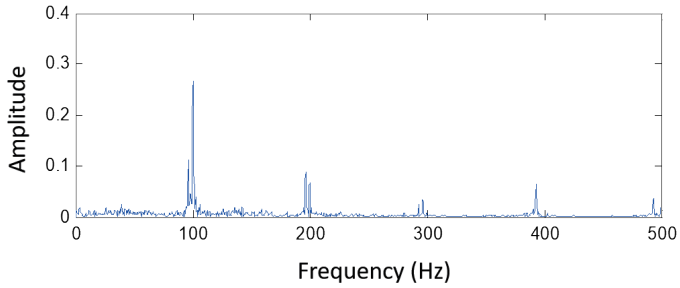

Fig. 9. (Color online) Envelope spectrum of *w*.

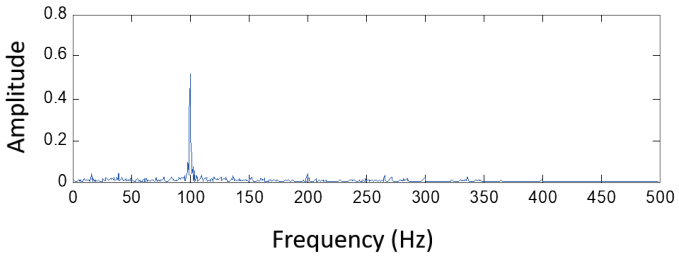

Fig. 10. (Color online) Envelope spectrum of *s*.

Table 2
Specifications of bearings used in experiment.

Position	Model	Manufacturer	Type	Application	Usage
Drive end	SKF 6205	SKF (Svenska Kullagerfabriken AB, Sweden)	Deep Groove Ball Bearing, 6200 Series	Widely used in electric motors, pumps, and machinery	Standard radial bearing with good load capacity
Fan end	SKF 6203	SKF (Svenska Kullagerfabriken AB, Sweden)	Deep Groove Ball Bearing, 6200 Series	Commonly used in smaller motors and auxiliary equipment	Compact size for lighter loads

The data analyzed correspond to inner race faults in the drive-end bearing. The bearing operated at 1797 rotations per minute, with a sampling frequency of 12 kHz. The rolling element diameter was 7.938 mm, the number of balls was 9, the pitch diameter was 39 mm, and the rolling element contact angle was 0°. The fault frequency of the bearing inner ring was calculated as

$$f_{ir} = \frac{n}{2} f_r \left(1 + \frac{d}{D}\cos\theta\right), \tag{10}$$

where f_{ir} denotes the inner race fault frequency, n is the number of rolling elements, f_r is the rotational frequency of the shaft, d is the rolling element diameter, D is the pitch diameter, and θ is the contact angle.[27] The fault frequency of the inner ring was calculated as 162.2 Hz using Eq. (10). From the inner ring fault data file, 1200 pieces of data were intercepted as the original experimental data. Figure 11 shows the waveform of x.

4.2 Algorithm process

The original signal x was preprocessed using the EEMD algorithm, resulting in the decomposition of 11 IMFs. The last four IMFs exhibited weak correlation with x and showed negligible amplitudes. Therefore, they were excluded from subsequent analysis. The ASAM values of IMF1–IMF8 were calculated, and the results are summarized in Table 3.

The deviation of the ASAM value from zero increased sharply after IMF4, while for IMF1–IMF3, it remained close to zero. Accordingly, IMF1–IMF3 were identified as high-frequency components and used to reconstruct the signal, denoted as k. A five-level wavelet decomposition was then applied to k, and the improved wavelet threshold algorithm was used to generate the final signal w. Figure 12 shows the waveform of k, and Fig. 13 shows the waveform of w.

To evaluate the fault detection performance, envelope spectrum analysis was conducted. Figure 14 presents the envelope spectrum of w, where a distinct pulse signal appears near the bearing inner ring fault frequency (162 Hz), along with its second ($2f$), third ($3f$), and fourth ($4f$) harmonics. This indicates strong fault-related features. For comparison, envelope spectrum

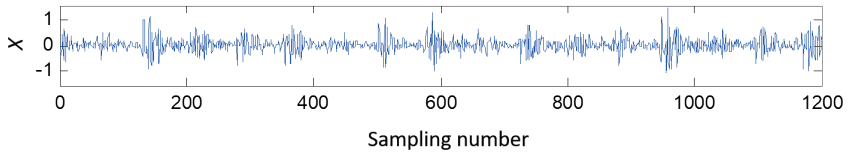

Fig. 11. (Color online) Signal waveform of x.

Table 3
ASAM values for EEMD results.

	IMF1	IMF2	IMF3	IMF4	IMF5	IMF6	IMF7	IMF8
ASAM ($\times 10^{-2}$)	−0.016	−0.48	−0.96	−3.18	−2.72	−4.57	−22.6	−49.8

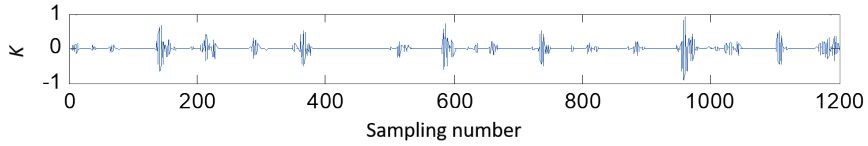

Fig. 12. (Color online) Waveform of reconstructed signal k obtained from IMF1–IMF3 decomposition.

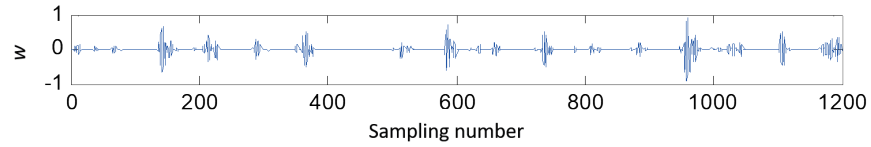

Fig. 13. (Color online) Waveform of the final denoised signal w after adaptive wavelet thresholding.

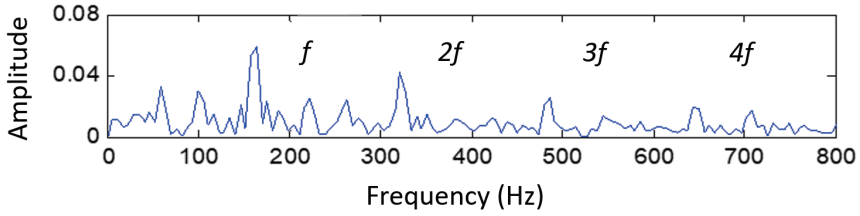

Fig. 14. (Color online) Envelope spectrum of denoised signal w, indicating the inner ring fault frequency (100 Hz) and its higher harmonics.

analysis was also performed on x, which was not processed for fault feature extraction. As shown in Fig. 15, although the fault frequency (162 Hz) is visible, its prominence is weak, and the harmonics are indistinct owing to noise interference. This demonstrates the superior noise suppression and feature enhancement capabilities of the proposed smart sensing framework.[6]

5. Discussion

The wavelet thresholding algorithm enhances the reliability of bearing fault diagnosis in high-noise environments. By isolating the fundamental fault frequency and its corresponding harmonics, the algorithm solves the information loss problem inherent in traditional denoising methods.

The algorithm precisely extracts the envelope spectrum of the inner ring fault. The ability to identify high-order transients enables a granular assessment of fault severity, shifting the diagnostic capability from simple failure detection to prognostic health monitoring.

Modern high-fidelity sensors, such as high-frequency piezoelectric accelerometers and MEMS-based vibration nodes, are designed to capture subtle transients associated with incipient mechanical failure. However, increased sensor sensitivity results in capturing environmental and electromagnetic noise. The developed algorithm acts as a signal-conditioning layer that enhances the availability of the output of the sensor components. In smart sensors and IoT, where data is

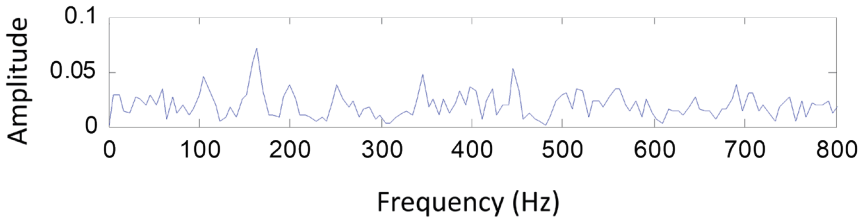

Fig. 15. (Color online) Envelope spectrum of original unprocessed signal x showing the masking effect of background noise on fault harmonics.

processed at the edge, the computational efficiency of the modified wavelet threshold is vital for embedding advanced diagnostics directly into the sensor firmware. This reduces the bandwidth required for data transmission and improves the real-time response of automated monitoring systems.

The results of the experiment with the CWRU data show that the algorithm outperforms traditional EMD and VMD in terms of spectral clarity and noise suppression. While EMD is prone to mode mixing and VMD requires precise presetting of the penalty factor and component number, the developed algorithm adaptively responds to the statistical nature of the signal through kurtosis integration. This robustness is important for the network where sensors are deployed under variable-speed or nonstationary operating conditions. The algorithm also maintains diagnostic accuracy despite the presence of significant additive noise, which shows its readiness for industrial integration.

However, the current algorithm detects single-point pitting faults. This necessitates further research to enhance its detection ability of multicomponent compound faults from multiple vibration sources. As sensor technology advances to multimodal fusion (combining vibration, temperature, and acoustic emission), the wavelet framework that handles synchronized multichannel sensor data can be used for effective machine health management.

6. Conclusions

In this study, a sensing framework was designed to elevate the functional intelligence of advanced vibration sensors used in industrial monitoring. By integrating a kurtosis-guided adaptive wavelet thresholding method directly into the signal acquisition chain, raw vibration transducers can be transformed into smart sensing nodes capable of autonomous noise suppression. This approach is significant for the development of edge-computing sensors, as it enables the high-fidelity extraction of incipient fault features without the need for massive off-site data processing. The results indicate that the proposed sensing concept effectively preserves the integrity of fault-related transients while mitigating the impact of harsh industrial background noise. Through the integration of kurtosis and decomposition level into the threshold calculation, the algorithm improves its adaptability to the denoising process. While traditional methods utilize fixed thresholds, the algorithm adjusts to the impulsive characteristics of the fault. In simulations utilizing noise profiles, the algorithm accurately identified the fault frequency of 100 Hz along with its higher-order harmonics, which are important for assessing fault severity

and type. The outcome of the algorithm shows a significant improvement over standard VMD and wavelet techniques that have information loss or spectral aliasing under heavy noise. By preserving harmonic characteristic markers that are typically lost in the traditional methods, the algorithm enhances the early warning capabilities of vibration monitoring systems. The developed algorithm enables a robust mathematical framework that is less computationally intensive than complex morphological operators, making it well-suited to the integration into the next-generation smart sensor firmware and industrial IoT (IIoT) nodes. Further studies are necessary to apply the adaptive thresholding framework to multisensor environments and combine vibration data with acoustic emission sensors. This is expected to enhance the reliability of machine health monitoring in a complex industrial environment.

References

1 X. M. Yang, Y. Guo, T. Tian, and Y. G. Guo: J. Vib. Shock **42** (2023) 67. https://doi.org/10.13465/j.cnki.jvs.2023.010.009
2 F. Jia, Y. Lei, H. Shan, and J. Lin: Sensors **15** (2015) 29363. https://doi.org/10.3390/s151129363?urlappend=%3Futm_source%3Dresearchgate.net%26utm_medium%3Darticle
3 C. Zhang and J. J. Chen: Mech. Sci. Technol. Aerosp. Eng. **34** (2014) 252. https://doi.org/10.13433/j.cnki.1003-8728.2015.0220. https://dx.doi.org/10.13433/j.cnki.1003-8728.2015.0220
4 G. Wu, T. Yan, G. Yang, H. Chai, and C. Cao: Sensors **22** (2022) 8330. https://doi.org/10.3390/s22218330
5 Z. Wu and N. E. Huang: Adv. Adapt. Data Anal. **1** (2009) 1. https://doi.org/10.1142/S1793536909000047
6 H. Gruberm A. Fuchs, and M. Bader: Sensors **24** (2024) 2138. https://doi.org/10.3390/s24072138
7 H. Tao, J. Qiu, Y. Chen, V. Stojanovic, and L. Cheng: J. Franklin Inst. **360** (2023) 1454. https://doi.org/10.1016/j.jfranklin.2022.11.004
8 C. Sun, H. Li, C. Xu, L. Ma, and H. Li: IEEE Sig. Proc. Let. **31** (2023) 216. https://doi.org/10.1109/LSP.2023.3347146
9 C. J. Li, Z. Cao, S. L. Li, and J. S. Dai: IEEE Sensors J. **24** (2024) 449. https://doi.org/10.1109/JSEN.2023.3331355
10 X. Dai and Z. Gao: IEEE Trans. Ind. Inform. **9** (2013) 2226. https://doi.org/10.1109/TII.2013.2243743
11 Y. Wang, Z. He, and Y. Zi: Mech. Syst. Signal Process. **24** (2010) 119. https://doi.org/10.1016/j.ymssp.2009.06.015
12 I.-S. Gherghina, N. Bizon, G.-V. Iana, and B.-V. Vasilică: Machines **13** (2025) 815. https://doi.org/10.3390/machines13090815
13 L X. Yang, R. Hou, C. Liu, and S. Liu: J. Vib. Eng. Technol. **14** (2026) 69. https://doi.org/10.1007/s42417-025-02185-x
14 M. A. Hossain, M. R. Islam, and M. S. Kaiser: Sensors **21** (2021) 1234. https://doi.org/10.3390/s21041234.
15 Z. Dong, S. Tian, J. Guo, Z. Meng, and F. Gu: J. Vib. Eng. **36** (2023) 1447. https://zdxb.nuaa.edu.cn/zdgcxb/article/pdf/202305029
16 A. Chennana, A. C. Megherbi, N. Bessous, S. Sbaa, A. Teta, E. O. Belabbaci, A. Rabehi, M. Guermoui, and T.F. Agajie: Sci. Rep. **15** (2025) 9270. https://doi.org/10.1038/s41598-025-93133-y
17 Y. Yan, C. Xu, X. Cheng, and J. Li: J. Vib. Shock **42** (2023) 118. https://jvs.sjtu.edu.cn/EN/Y2023/V42/I15/118
18 (G6) Y. Sato and H. Nakamura: Sens. Mater. **36** (2024) 102. https://doi.org/10.18494/SAM.2024.0102
19 K. Cui, M. Liu, and Y. Meng: Meas. Sci. Technol. **35** (2024) 076108. https://doi.org/10.1088/1361-6501/ad3456
20 X. Wang, J. Feng, J. Liu, and E. Xing: J. Optoelectron,. Laser **34** (2023) 734. http://joelcn.ijournals.cn/gdzjg/article/abstract/20230708?st=search
21 D. L. Donoho and I. M. Johnstone: Biometrika **81** (1994) 425. https://doi.org/10.1093/biomet/81.3.425
22 C. Lei. C. Miao, H. Wan, J. Zhou, D. Hao, and R. Feng: Meas. Sci. Technol. **35** (2024) 035007. https://doi.org/10.1088/1361-6501/ad11c7
23 L. Jiao and J. Ma: Proc. 9th Data Driven Control and Learning Systems Conf. (DDCLS, 2020) 167. https://doi.org/10.1109/DDCLS49620.2020.9275058
24 X. Li, K. Liao, G. He, and J. Zhao: Electronic **12** (2023) 1244. https://doi.org/10.3390/electronics12051244
25 Case Western Reserve University: https://engineering.case.edu/bearingdatacenter/download-data-file (accessed March 2026).
26 W. A. Smith and R. B. Randall: Mech. Syst. Signal Process. **64–65** (2015) 100. https://doi.org/10.1016/j.ymssp.2015.04.021
27 P. D. McFadden and J. D. Smith: J. Sound Vib. **96** (1984) 69. https://doi.org/10.1016/0022-460X(84)90595-9